

REPORT DOCUMENTATION PAGE				Form Approved OMB No. 0704-0188	
<p>The public reporting burden for this collection of information is estimated to average 1 hour per response, including the time for reviewing instructions, searching existing data sources, gathering and maintaining the data needed, and completing and reviewing the collection of information. Send comments regarding this burden estimate or any other aspect of this collection of information, including suggestions for reducing the burden, to Department of Defense, Washington Headquarters Services, Directorate for Information Operations and Reports (0704-0188), 1215 Jefferson Davis Highway, Suite 1204, Arlington, VA 22202-4302. Respondents should be aware that notwithstanding any other provision of law, no person shall be subject to any penalty for failing to comply with a collection of information if it does not display a currently valid OMB control number.</p> <p>PLEASE DO NOT RETURN YOUR FORM TO THE ABOVE ADDRESS.</p>					
1. REPORT DATE (DD-MM-YYYY) 03/28/2014		2. REPORT TYPE Final Technical Report		3. DATES COVERED (From - To) 7/2/2012 - 12/31/2013	
4. TITLE AND SUBTITLE Final Technical Report of ONR Grant N00014-12-1-0921  Feasibility study of Compressive Sensing Underwater Imaging Lidar				5a. CONTRACT NUMBER	
				5b. GRANT NUMBER N00014-12-1-0921	
				5c. PROGRAM ELEMENT NUMBER	
6. AUTHOR(S) Bing Ouyang				5d. PROJECT NUMBER 040313	
				5e. TASK NUMBER	
				5f. WORK UNIT NUMBER	
7. PERFORMING ORGANIZATION NAME(S) AND ADDRESS(ES) Harbor Branch Oceanographic Institute at Florida Atlantic University 5600 US Hwy 1 North, Fort Pierce, FL 34946				8. PERFORMING ORGANIZATION REPORT NUMBER 040313	
9. SPONSORING/MONITORING AGENCY NAME(S) AND ADDRESS(ES) Office Of Naval Research 875 North Randolph St. Arlington, VA 22203-1995				10. SPONSOR/MONITOR'S ACRONYM(S) ONR	
				11. SPONSOR/MONITOR'S REPORT NUMBER(S)	
12. DISTRIBUTION/AVAILABILITY STATEMENT DISTRIBUTION STATEMENT A. Approved for public release; distribution is unlimited.					
13. SUPPLEMENTARY NOTES					
14. ABSTRACT <p>This project supported the feasibility study of a compressive line sensing underwater imaging system concept through a series of theoretical work, simulations and experimental studies.</p> <p>This project supports an overarching research goal of developing a compressive sensing theory based extended range underwater electro-optical sensor that is compact, cost effective, energy efficient and highly adaptive to the environment and tasks. Such system can be advantageous when conducting EOID using high speed AUV.</p>					
15. SUBJECT TERMS Compressive Sensing, underwater electro-optical imaging system, laser, active imaging system					
16. SECURITY CLASSIFICATION OF:			17. LIMITATION OF ABSTRACT	18. NUMBER OF PAGES	19a. NAME OF RESPONSIBLE PERSON
a. REPORT	b. ABSTRACT	c. THIS PAGE			Bing Ouyang
Statement A	Statement A	Statement A	SAR	25	19b. TELEPHONE NUMBER (Include area code) 772-242-2288

## Final Technical Report of ONR Grant N00014-12-1-0921

### Feasibility study of Compressive Sensing Underwater Imaging Lidar

Bing Ouyang

phone: (772) 242-2288 fax : (772) 242-2257 email: [bouyang@hboi.fau.edu](mailto:bouyang@hboi.fau.edu)

Fraser R. Dalgleish

phone: (772) 242-2591 fax : (772) 242-2257 email: [fdalglei@hboi.fau.edu](mailto:fdalglei@hboi.fau.edu)

Anni K. Vuorenkoski

phone: (772) 242-2477 fax : (772) 242-2257 email: [adalglei@hboi.fau.edu](mailto:adalglei@hboi.fau.edu)

Harbor Branch Oceanographic Institute at Florida Atlantic University  
5600 US Hwy 1 North, Fort Pierce, FL 34946

<http://www.fau.edu/hboi/>

March 2014

#### ABSTRACT

This final technical report describes the efforts during the interval from July 2012 through the end of December 2013 to accomplish the project objective of studying the feasibility of developing a compressive sensing theory based approach to form a grayscale image in the underwater environment.

This objective was accomplished through a series of theoretical work, simulations and experimental studies. In the first stage of this project, the frame based Compressive Sensing underwater imaging system concept was further studied. This study resulted in a publication that was among the top most downloaded papers on the Journal of Electronic Imaging website until November 2013. One of the most important achievements of the project is that the Compressive Line Sensing underwater imaging system was conceptualized. Built upon the theoretical foundation the Compressive Sensing theory and the Distributed Compressive Sensing theory, this technique employs the paradigm of *independently* sensing each line and *jointly* reconstructing a group of line. Such implementation is compatible with the traditional whiskbroom type survey, but achieves significant *resource compression* by exploiting the correlation/redundancy among adjacent target regions. An image reconstruction framework was developed based on this concept. Extensive simulations were conducted to validate this framework. A prototype system was developed to further validate the Compressive Line Sensing framework through the experimental study. A journal paper describing this effort will be published in Journal of Optical Engineering special section on ocean optics.

20151007656

## Table of Contents

	<u>Page</u>
1. OBJECTIVES	2
2. APPROACH	2
3. WORKS COMPLETED	3
4. RESULTS	10
5. CONCLUSIONS	21
6. REFERENCES	23
7. RELATED PROJECTS	24
8. PUBLICATIONS ACKNOWLEDGING ONR GRANT N00014-12-1-0921	25
9. PATENTS	25

### **1. OBJECTIVES**

The main objective of the project is to study the feasibility of applying the compressive sensing theory to develop an alternative approach to form a grayscale image in the underwater environment.

This project supports an overarching research goal of developing an extended range underwater electro-optical imaging system that is compact, cost effective, energy efficient and highly adaptive to the environment and tasks. Such system can be advantageous when conducting electro-optical identification (EOID) using high speed Autonomous Underwater Vehicle (AUV) in a constant varying environment such as the turbid coastal zone.

### **2. APPROACH**

To achieve the project objective, the PIs engaged in a number of activities over the course of eighteen months. The sensing process of a compressive sensing imaging system in a scattering environment was studied.

Based on the understanding of this sensing process, we first developed the system architecture of a frame based compressive sensing underwater imaging system. This system concept assumes a stationary sensing platform and utilizes COTS solid state Spatial Light Modulation (SLM) device [8] that can switch among many patterns at very fast rate. A series of simulations and experimental work were conducted to study this system concept.

The novel Compressive Line Sensing system concept was developed next. This technique retained the basic design of the aforementioned frame based system. One significant difference is that the system removes the requirement of a stationary platform and is more compatible the whiskbroom imaging formation mode employed in most traditional electro-optical survey operations. Adopting the paradigm of “*independently* sensing each line and *jointly* reconstruct a group of lines” enabled by the Distributed Compressive Sensing theory, the system maintains good image quality at high compression ratio. The feasibility of the proposed Compressive Line Sensing system concept was validated through a series of simulations and the initial experimental study using a prototype constructed with a Texas Instruments Digital Micromirror Devices development system.

In addition, through these studies, the deficiencies and/or areas of lack understanding can be identified and addressed in future work.

### 3. WORKS COMPLETED

#### 3.1. Foundation of the compressive sensing underwater imaging system

As the first step in the investigation, the theoretical foundation of the proposed imaging system concept was established.

##### Compressive Sensing and Distributed Compressive Sensing

One of the two theories that support the proposed concepts is the Compressive Sensing (CS) theory that defines a framework for the *simultaneous sampling and compression* of sparse signals using incomplete linear measurements [1, 3-6]. While CS theory mostly addresses the intra-signal sparsity, the Distributed Compressive Sensing (DCS), closely related to the distributed source coding theorem [15, 18], attempts to additionally exploit the inter-signal redundancy among distributed and correlated sources through the establishment of the proper joint sparsity models (JSMs). Among the three different joint sparsity models proposed in Baron et al. [2], JSM-1 is of primary interest in this study. In the JSM-1 framework, each signal  $X_l$  within the group is the sum of a common component  $Z_c$  and a component that is unique to each signal  $Z_l$ :  $X_l = Z_c + Z_l$ ,  $l = 0, 1 \dots L$ , where  $L$  is the number of signals to be solved jointly via  $L1$  minimization. Among the several  $L1$  minimization software packages evaluated,  $L1\_homotopy$  [19] was selected for this project. One of the attractive features of  $L1\_homotopy$  is that it supports the reweighted  $L1$  minimization [5].

##### Impact of the underwater environment on the sensing process

Compared to over-the-air scenarios, the main challenge for the underwater CS imagers is the pronounced beam spreading and attenuation due to the propagation of light through the scattering and absorbing ocean water, (we ignore the effects of solar irradiance/ambient light in the current study). When a binary pattern of highly collimated light is emitted from the transmitter, the light will diffuse and attenuate as it propagates to the target plane. The degree of spreading/attenuation is determined by the laser beam divergence, target range, and the inherent optical properties of the water. The target scene reflection is given by the product of the incident light pattern and the surface reflectivity pattern  $X$  of the scene. The reflected light will then undergo additional spreading and attenuation as it propagates to the PMT receiver. The photon flux corresponding to the target scene reflection that enters the receiver is a function of the PMT location and orientation, its sensitivity pattern, and the inherent optical properties. The (non-target information bearing) photon flux due to volume backscatter in the water will also contribute to the measured signal.

Assuming a wide receiver aperture and Lambertian reflection at the scene, the total photon flux corresponding to the  $m^{th}$  measurement  $y_m$  can be represented by the equation (\* denotes convolution and  $\circ$  represents the Hadamard point-by-point product):

$$y_m = P_{sys} \left( \frac{\alpha_{TR}}{N_{1,m}} \sum_{i,j} [\Phi_m(i,j) \circ X(i,j)] + \hat{\beta}_m \right) \quad (1)$$

where  $P_{sys}$  is a constant accounting for certain system specifications (receiver aperture, power etc.);  $\alpha_{TR}$  is an attenuation coefficient related to radiative transfer from the scene back to the sensor;  $N_{1,m}$  is the number of ‘on’ pixels in the illumination pattern  $m$ ;  $\Phi_m = A_m * BSF_{IT}$  is the measurement pattern on the target plane (i.e., the original binary pattern after propagating from the illuminator to the target plane through a scattering and absorbing medium described by the beam spread function  $BSF_{IT}$ );  $\Phi_m \circ X$  is the (information bearing) “imprinted” pattern due to the modulation of the measurement pattern by the target scene reflectance pattern;  $y_m$  is the corresponding total reflected photon flux. Making the reasonable assumption that the volume backscatter contribution from every beam ( $\hat{\beta}$ ) in



the illumination pattern is the same; the total volume backscatter component of the measurement is proportional to the number of “on” pixels in the pattern  $N_1$ .

Three key observations can be drawn from Equation (1):

- I) The measurement matrix  $\{\Phi_m\}$  corresponding to a dense binary illumination patterns  $A_m$  represents a loss of detail due to the low-pass filtering effect of the  $BSF_{IT}$  (Figure 1).

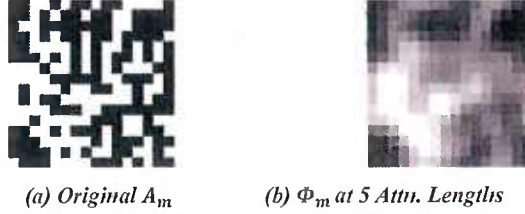


Figure 1. Binary illumination pattern and measurement matrix in turbid water.

- II) The modulation occurs between the target scene reflectance patterns and  $\Phi_m$  instead of  $A_m$ .
- III) The impact due to the propagation from the target to the receiver on the total photon flux is essentially diffuse attenuation that can be represented by an attenuation factor  $\alpha_{TR}$ , which remains unchanged for all the patterns in the sensing process.

#### Measurement matrix design and image reconstruction for compressive sensing underwater imager

The underwater compressive sensing system design incorporates three components to address the aforementioned issues:

*Model assisted reconstruction:* the Electro-Optical Detection Simulator (EODES) radiative transfer models [9] have been extended to predict the on-target sensing patterns  $\{\Phi_m\} = \{A_m\} * BSF_{IT}$ , which are used in the image reconstruction process;

*Multi-scaled binary pattern:* To mitigate the forward scattering and backscattering, multi-scale binary dither patterns (Figure 2) are adopted. Each pattern is divided into  $N_b \times N_b$  level one blocks (Figure 2(a)). Only one “on” pixel is present within each block, and its in-block location follows an uniform distribution (Figure 2(b)). The on/off polarity of a block is determined by an independent Bernoulli random variable.

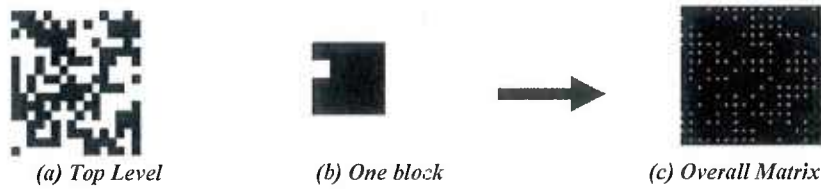


Figure 2. Multi-scale measurement matrix.

*Bipolar matrices and measurements via polarity flipping:* During image reconstruction, the positive-valued (EODES model predicted) measurement matrices  $\{\Phi_m\}$  and the raw measurements  $\{y_m\}$  will be converted to bipolar matrices  $\{\Phi_m^B\}$  and vectors  $\{y_m^B\}$ , where  $B$  indicates that both positive and negative values are possible. In hardware, each dither pattern is loaded twice, first with the DMD mirrors “on” (corresponding to a digital “1”) only in the blocks originally chosen to be “on”, producing the pattern  $\Phi_m^+$ , and then with mirrors “on” only in the blocks originally selected to be “off”, producing  $\Phi_m^-$  (Figure 4). The relations

$$\begin{aligned}\Phi_m^B &= C(\Phi_m^+ - \Phi_m^-) \\ y_m^B &= y_m^+ - y_m^-\end{aligned}\tag{2}$$

where  $y_m^+$  and  $y_m^-$  are the measurements corresponding to  $\Phi_m^+$  and  $\Phi_m^-$ , represent the sensing process when polarity flipping is employed.

The  $L1$ -minimization problem becomes:

$$\begin{aligned} \alpha^* &= \arg \min \|\alpha\|_1 \\ \text{subject to } \|\mathbf{y}^B - \Phi^B \Psi \alpha\|_2 &= \|\mathbf{y}^B - (A^B * BSF_{IT}) \Psi \alpha\|_2 \leq \varepsilon \end{aligned} \quad (3)$$

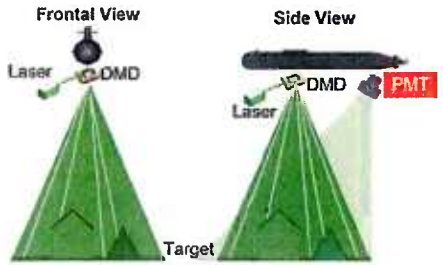
where  $\mathbf{y}^B = \{y_m^B\}$ ,  $A^B = \{A_m^B\}$  and  $\Phi^B = \{\Phi_m^B\}$ .

One difference between Equation (3) and the  $L1$  minimization cost function for the normal CS problems is the incorporation of the convolution in the constraint term in Equation (3) to more accurately reflect the sensing process in the scattering medium. In essence, Equation (3) can be regarded as *simultaneous compressive sensing and deconvolution*.

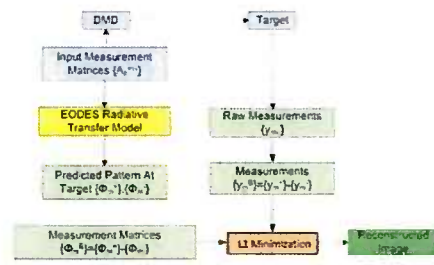
With this foundation, two underwater compressive sensing concepts have been developed. We will first discuss the concept of a frame based system that assumes the illuminator and receiver are located on stationary platforms during the sensing process.

### 3.2 Frame-based compressive sensing imaging system design

The proposed frame-based CS underwater laser imager is an active serial imaging system. The overall system processing flow is illustrated below in Figure 3(b). During the sensing process, a sequence of pre-generated binary illumination patterns  $\{A_m\}$  is loaded onto a Spatial Light Modulation (SLM) device, such as the Digital Micromirror Device (DMD), to spatially modulate the laser source that illuminates the target plane. The same binary patterns are also submitted to a radiative transfer model such as EODES to predict the measurement matrix  $\{\Phi_m\}$  at the target plane. At the receiver, a “bucket” photon collector such as the PMT records the total optical return signal. The difference between polarity-flipped pairs of measurement matrices constitutes  $\{\Phi_m^B\}$  is one input to the reconstruction process. The difference between their corresponding PMT measurements  $\{y_m^B\}$  is the other input to the reconstruction process.



(a) Illustration of the sensing process



(b) System flow chart

Figure 3. Frame based compressive sensing underwater laser imager

### 3.3 Simulation Environment

The core of the simulation environment was the EODES radiative transfer model. Both the image simulation tool EODES-I (for fast simulation speeds) and the temporal simulation tool EODES-T (providing more accurate results) were utilized to construct the CS simulation environment (Figure 4).

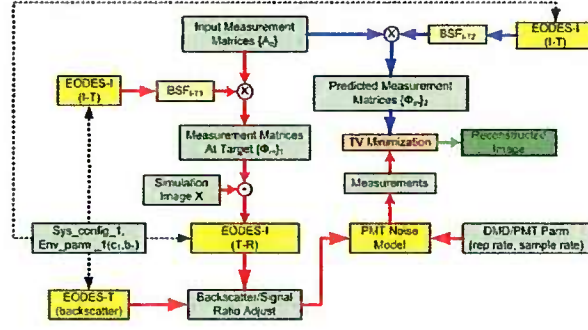


Figure 4. Simulation flow.

Different beam attenuation ( $c$ ) and/or scattering ( $b$ ) coefficients can be specified for the simulation path (red arrows) and the model-prediction path (blue arrows) when predicting the measurement matrices using the EODES-I model. The same system and environmental parameters are used as input to the EODES-T temporal model to derive a more accurate backscatter and signal levels. A Metron-developed PMT Noise Model was adopted to model the receiver noise performance [10, 14]. The simulation environment undergoes iterative enhancements to improve the fidelity of the simulation results.

### 3.4 Compressive Line Sensing imaging system design

#### Sensing process in a compressive line sensing underwater imaging system

For conventional underwater survey, the platforms are generally moving at uniform speed in a “lawn mow” pattern and the images are acquired line by line in a whiskbroom fashion. Therefore, it is desirable to extend the aforementioned frame-based design to a line-based system. In this regard, we rewrite Equation (3):

$$y_m(L + \Delta L_m) = P_{sys} \left( \frac{\alpha_{TR}}{N_{1,m}} \sum_{j=-U}^U \sum_{i=1}^N [(BSF_{IT}(i,j) * A_m(i,j)) \circ X(i, L + \Delta L_m - j)] + \hat{\beta}_m \right) \quad (4)$$

where  $L$  is the current line under investigation;  $U$  is the effective vertical aperture due to the spreading in the vertical (along track) direction (i.e., the full width at half maximum of the vertical aperture);  $N$  is the number of pixels within each line;  $\Delta L_m = mv\Delta t$  is the platform displacement when the measurement pattern  $m$  is projected (relative to the previous pattern);  $\Delta t$  is the refresh time of the SLM device and  $v$  is the platform speed. The platform motion provides the second axis in the image formation (i.e. sensing next line). In this regard, the compression ratio:  $\frac{\text{Pixel/line (N)}}{\text{Measurements/line (M)}}$  is proportional to the platform speed; that is, the measurement rate (i.e., the number of measurements that can be taken within the line sensing time) is inversely proportional to the platform speed.

It can be observed by comparing Equation (4) with Equation (1) that the essential sensing process remains similar; therefore, the general principles developed for the frame-based system design are still valid for line-based sensing. Namely, the model-assisted reconstruction and the multi-scale, polarity flipping based bipolar measurement matrix design carry over to the line-based sensing paradigm. Nevertheless, in addition to the fact that the illumination patterns will be 1D instead of 2D, there are some new challenges in a line-based implementation. The reconstruction of each line can be treated as an independent CS problem. However, since in most natural scenes the adjacent lines are highly correlated, techniques that also exploit the joint sparsity such as DCS offer the potential to take advantage of this correlation to achieve improved image quality at the same measurement rate. In particular, the DCS *JSM-I*, which exploits the sparsity of a group of sources (i.e., lines) by modeling

them as consisting of a common component and unique components for each line, is deemed suitable for the current application.

To better understand how to map the current problem into the joint sparsity framework, we will develop the measurement model with certain simplifications. First, we concentrate on the scenario where the refresh rate of the SLM device is sufficiently fast relative to the platform motion. In this case, the displacement  $\Delta L_m$  is sufficiently small during the time to acquire the measurements needed to recover a single line:

$$y_m(L) \approx P_{sys} \left( \frac{\alpha_{TR}}{N_{1,m}} \sum_{j=-U}^U \sum_{i=1}^N [(BSF_{IT}(i,j) * A_m(i,j)) \circ X(i, L-j)] + \hat{\beta}_m \right) \quad (5)$$

We assume that the platform speed is constant; therefore, the same number of measurements will be taken for each line. We will further make a reasonable approximation that the beam spread function has a separable kernel that can be decomposed into:  $BSF_{IT} \approx B^H B^V$ , where  $B^V$  and  $B^H$  describe the vertical and horizontal beam spreading respectively. Taking into consideration that  $A_m$  is now a one-dimensional (1D) pattern, Equation (5) can be simplified to:

$$\begin{aligned} y_m(L) &\approx P_{sys} \left( \frac{\alpha_{TR}}{N_{1,m}} \sum_{j=-U}^U \sum_{i=1}^N (B^V B^H * A_m(L)) \circ X + \hat{\beta}_m \right) \\ &= P_{sys} \left( \frac{\alpha_{TR}}{N_{1,m}} \sum_{j=-U}^U B^V(j) \circ \left( \sum_{i=1}^N \Phi_m^H(L, i) \circ X(i, L-j) \right) + \hat{\beta}_m \right) \end{aligned} \quad (6)$$

where  $\Phi_m^H(L) = B^H * A_m(L)$  is the sensing pattern after undergoing horizontal spreading and the index in  $A(L)$  and  $\Phi(L)$  indicates they are the patterns for line  $L$ . Equation (6) essentially represents a convolution of the measurements of each cross-track line with the vertical (along-track) beam spreading  $B^V$ . Figure 4 is a graphical description of the measurement model based on Equation (6). It illustrates a new challenge in the compressive line sensing: because of vertical spreading, the measurement matrix is not of the diagonal block matrix form that most joint sparsity models assume.

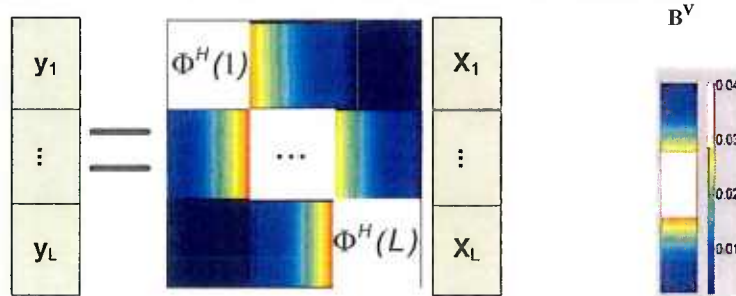


Figure 4. Compressive line sensing measurement model

With the further approximation of ignoring the vertical spreading, the non-diagonal blocks are set to zero and the measurement matrix for DSC JSM-1 will take the form:

$$\tilde{\Phi}^B = \begin{bmatrix} \Phi^{HB}(1) & \dots & 0 & \Phi^{HB}(1) \\ \vdots & \ddots & \vdots & \vdots \\ 0 & \dots & \Phi^{HB}(L) & \Phi^{HB}(L) \end{bmatrix}$$



where the superscript  $B$  indicates the application of Equation (2) to obtain the bipolar signal. The corresponding cost function is:

$$\begin{aligned} \alpha^* = \arg \min & \|a_c\|_1 + \|a_1\|_1 + \dots + \|a_L\|_1 \\ \text{subject to } & \|\tilde{y}^B - \tilde{\Phi}^B \Psi a\|_2 = \|\tilde{y}^B - (\tilde{A}^B * B^H) \Psi a\|_2 \leq \varepsilon \end{aligned} \quad (7)$$

Evidently ignoring vertical spreading to comply with the joint sparsity model introduces additional interferences/errors, especially in high-turbidity cases. However, an interesting aspect of the compressive line sensing imager is that, with the continuous forward progress of the platform, each line can be included in as many as  $2U + 1$  different groups while it is inside the effective vertical aperture. Line groups with higher joint sparsity (i.e., lines within the group are more correlated) should result in a better solution. Therefore, it is beneficial to solve each line multiple times while it is inside the aperture, and select the best among all the runs as the final solution for that line. Buffering of the multiple solutions of the same line, therefore, provides an alternative way to exploit the line-to-line correlations. Various filters (i.e., median filtering, averaging etc.) can be applied to accomplish the “selection”.

#### Compressive line sensing imaging system processing flow

Based on the above analysis, the compressive line sensing imager design may be summarized. The system is consistent with those used for traditional survey operations (Figure 6b). The three components developed for the frame-based system (the model-predicted reconstruction; multi-scaled measurement matrices, and polarity flipping to construct bipolar measurements/matrices) are retained with the difference that the 1D patterns are generated by the SLM device. The illuminator of the compressive line sensing system shares some similarity with that of the Streak Tube Imaging Lidar (STIL) (McLean [12]) which deploys a 1D fan beam (wide cross-track, narrow along-track beam divergences) illumination. However, a *significant* difference is that instead of pulsing with uniform light as in STIL, the illumination scheme for a CS-based system consists of a line “patterns” generated via SLM, which are used to “encode” the current line (Figure 6a).

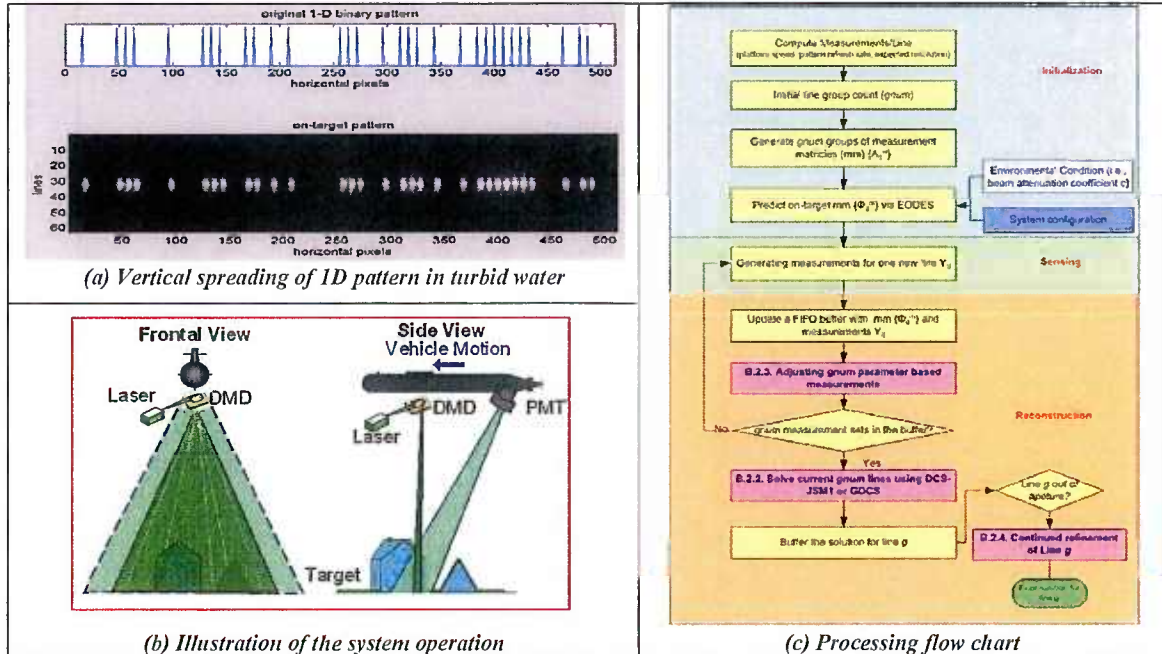


Figure 6 Illustration of the system operation and the processing flow chart of the Compressive Line Sensing Imager

The process flow is shown in Figure 6c. There are essentially three sections in the processing: initialization, sensing and reconstruction. During the initialization, the number of measurements per line is first computed from the given expected platform speed and the SLM refresh rate. The line group count ( $gnum$ ), which is the number of lines to be solved jointly, is determined according to the system specifications and environmental conditions, such as the water turbidity, target distance, laser divergence, etc. Adjusting this parameter during the operation, after some initial image quality evaluation, is a trivial process.

After the sensing of one line is accomplished, a first-in-first-out buffer that consists of  $gnum$  sets of measurements and measurement matrices will be updated with the new data. Subsequently, the group of lines in the buffer will be used to solve the L1\_homotopy problem. The resulting solutions for each line are also buffered. When a line moves out of the effective vertical aperture, filtering such as median filter can be applied to obtain the final solution:

$$X(L) = median[X^u(L)], \text{ for } u = 1 \dots 2U + 1 \quad (8)$$

where  $X^u(L)$  is the  $u^{th}$  solution for line  $L$ .

### 3.5 Compressive Line Sensing imaging system prototype

A prototype system has been developed for the initial experimental validation of the Compressive Line Sensing concept. The core of the illumination sub-system is the DLP Lightcrafter evaluation module, consisting of a 608 x 684 diamond pixel 0.3" WVGA DMD (Figure 7b). Also can be observed in Figure 7b, the system is very compact with a dimension of 117mm x 65mm x 23mm.

The overall prototype system is shown in Figure 7a. The configuration of the receiver was very straightforward – consisting of a Hamamatsu R9880U-210 PMT with 12 degree FOV. The output of the PMT was connected to a National Instruments PCI-6133 analog data acquisition board capable of A/D with 14 bit precision.

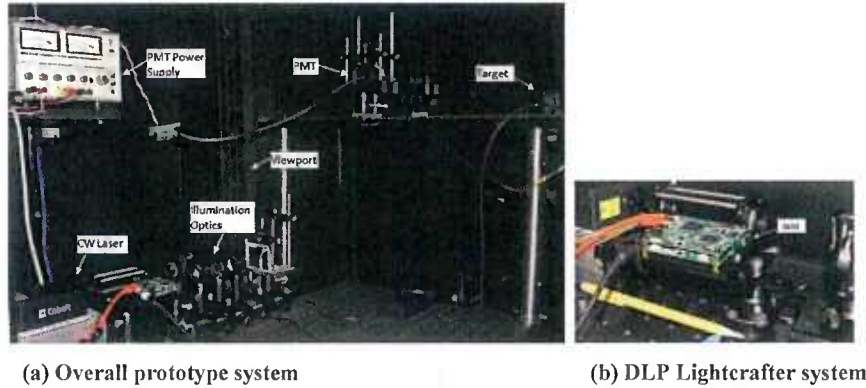
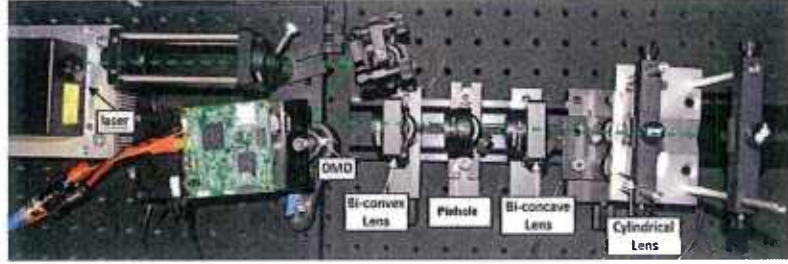


Figure 7. CLS prototyping system

The illuminator design, on the other hand, required significant effort. The illuminator needed to generate 1-D random patterns. Since the DMD is a 2-D SLM device, to achieve this objective, 2-D line patterns were fed into the Lightcrafter and focusing optics was designed to convert 2-D line patterns into 1-D (dot) patterns. One of the complicating factor was that due to the small pitches of the DMD mirrors ( $<10\mu m$ ), when illuminated with highly coherent laser, strong diffraction patterns would present (Figure 8a).



(a) DMD diffraction patterns from coherent laser illumination



(b) Illuminator optical design to mitigate the DMD diffraction

Figure 8. DMD diffraction and its mitigation

While it was possible to re-combine the different order diffraction patterns using more sophisticated optics (as in most DLP projection system), to simplify the design, a mechanical pinhole and a baffle were used to filter out all non-zero-order patterns. While the design was not very efficient (the power of the laser source was set to 1w; the maximum system output power was measured to be 90mw), it served the purpose of the initial validation prototype system. The resulting optics design is shown in Figure 8b. The original LED light engine of the Lightcrafter was removed to expose the DMD to external laser illumination. Beam expanding optics and reflecting mirror were used to focus laser beam from a Cobolt Samba CW laser onto the DMD surface. Along the “on” reflection path of the DMD, a series of optics (Bi-convex spherical lens, mechanical slit, bi-concave spherical lens and cylindrical lens) were used to filter out non-zero order diffraction patterns and convert the 2-D line patterns into 1-D dot patterns.

The original 2-D line pattern and the corresponding 1-D on-target pattern generated using the aforementioned illuminator design is shown in Figure 9 (ambient lighting was turned on when acquiring the on-target pattern for better rendition).



(a) 2-D line pattern fed into Lightcrafter



(b) Corresponding 1-D dot pattern

Figure 9. Original 2-D line pattern and on-target 1-D pattern

## 4. RESULTS

### 4.1. Simulation and experimental results of the frame-based system

Simulations were conducted for three different technologies: CS, Pulsed LLS (PLLS), Continuous Wave (CW) LLS. A near-monostatic configuration was adopted for all simulations. The laser and PMT separation was set to 0.4 m. The target panel was 1.2m<sup>2</sup> and located 7 m away from the illuminator-receiver assembly. The resolution of the image and the sensing patterns was 64×64 pixels. Average laser power was 4 W, and the DMD refresh rate was 4 kHz. For CS simulation, 1024 measurements were used (due to polarity flipping 2048 raw measurements were acquired), resulting in a compression ratio of 0.5. Since the illumination was frame based, the input power for each pixel element was set to  $P_{\text{pixel}} = P_{\text{total}}/(N^2\tau)$ , where  $N^2$  is the pixel count, to match the power levels in the PLLS and CW LLS simulations. In the PLLS simulations, a 3 ns laser pulse with 4 kHz repetition



rate ( $\tau$ ) was used and perfect range gating (i.e., no backscatter reached the PMT) was assumed. The receiver apertures were set to 15 *mrad* for the PLLS and CW LLS simulations, 90 *mrad* for the CS simulations. In the CS simulations, the pattern top level block size (i.e. minimum distance between two ON pixels) was set to four pixels. A noise factor  $NF = 1.2$  was assumed throughout the simulations. To evaluate the simulation image quality, a well-known image quality metric, the structural similarity index metric (SSIM) [17], was adopted.

### Simulation Results

Figures 10 and 11 demonstrate CS imager performance against various test images at different turbidities. These images consisted of both test patterns (Star Chart and Geometry patterns) and images taken in underwater environments (coral, fish, and diver). In Figure 11, the structural SSIM at various turbidities is presented.

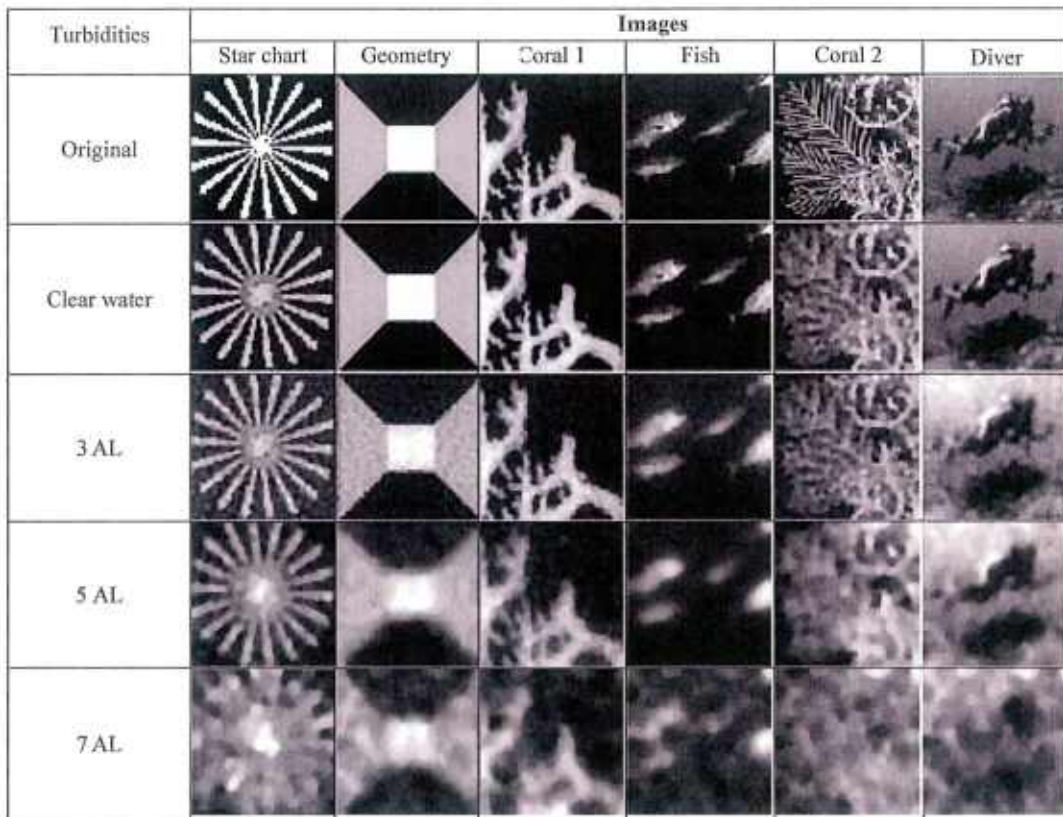


Figure10. Reconstruction images at different turbidities.



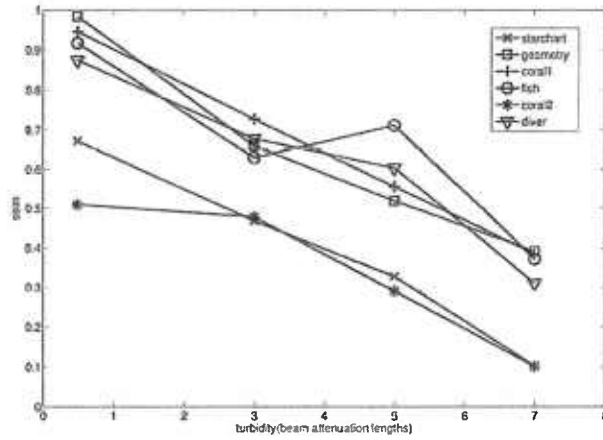
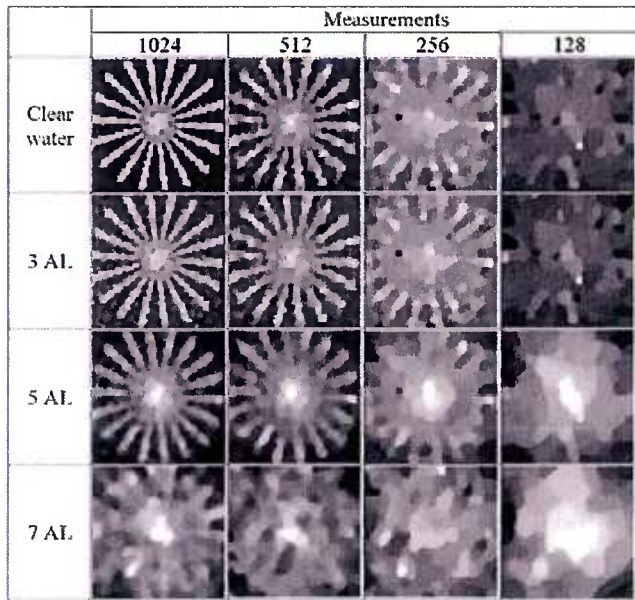


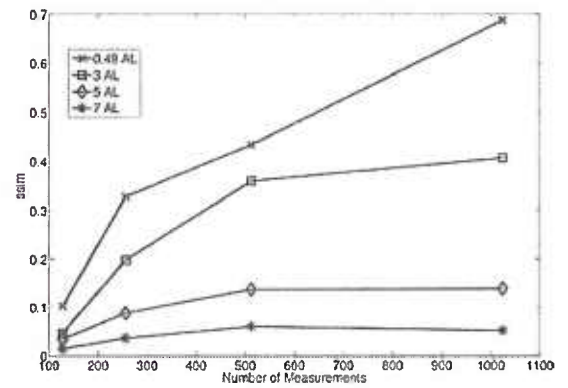
Figure11. Reconstruction Performance at different turbidities (SSIM metrics).

As seen from Figure 11, the quality degraded with increasing turbidity for all of the test images. One interesting observation was that the SSIMs for the Star Chart and Coral 2 were lower than those for the other patterns, which resulted in better performance of the TV minimization based optimization. At the range of 7 AL all test images suffered significant loss of detail, which was due to the noise interfering with the reconstruction.

Figure 12 illustrates the image quality change with different numbers of measurements (i.e., different compression ratios). It is interesting to note that there was more obvious image quality degradation with reduced measurements in clearer waters than at higher turbidities.



(a) Reconstructed images

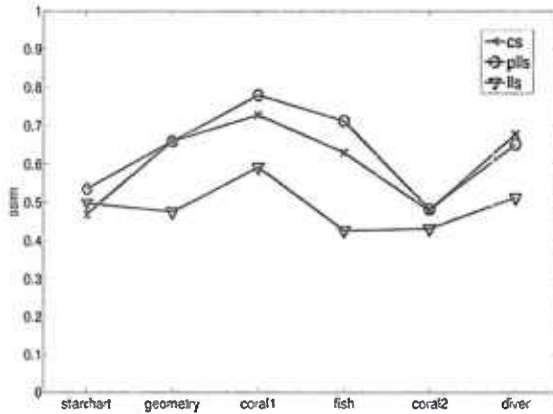


(b) Corresponding SSIM curves

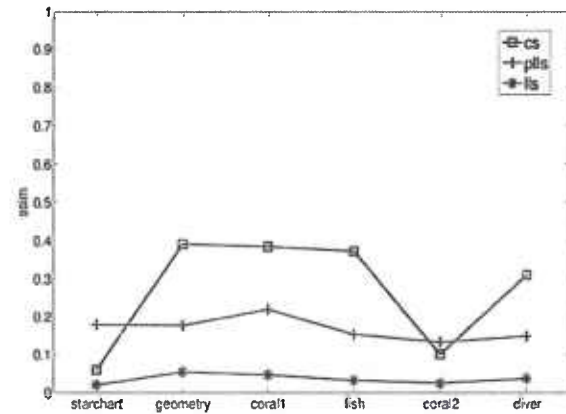
Figure12. Reconstruction performance with different number of measurements.

Turbidity	Technique	Images					
		Star chart	Geometry	Coral 1	Fish	Coral 2	Diver
3 AL	CS						
	PLLS						
	LLS						
7 AL	CS						
	PLLS						
	LLS						

(a) Simulated images at different turbidities using the three different techniques



(b) SSIM Curves with turbidity at 3 AL



(c) SSIM curves with turbidity at 7 AL

Figure13. Reconstruction performance at different turbidities.

The CS results were compared with the images from PLLS and CW LLS simulations in Figure 13. For the SSIM curves, the names of the test images are listed on the x-axis. It can be seen that the image quality of the CS imager was comparable to that of PLLS and LLS at lower turbidity (3 AL). At a higher turbidity (7 AL) the PLLS images preserved the image detail the best; CS images suffered more resolution loss than PLLS, especially for images with more high-resolution content; and, the

CW LLS images were overwhelmed by noise. One reason for the relatively poor performance of the CS imager at high turbidity was that the current image reconstruction model assumed an additive Gaussian noise corruption, which deviated from the true noise characteristics of the PMT receiver. It is conceivable that a reconstruction model that better reflects the PMT noise could significantly improve CS imager performance, especially at higher turbidities.

### Underwater Experimental Results

An underwater experiment was conducted in the HBOI optical test tank to validate the proposed frame-based compressive sensing serial imaging design. The target plane consisted of multiple technical targets (Geometry and Star Chart) and coral samples (Figure 14a). A LabView based data acquisition system was developed for this effort. A series of pre-generated illumination pattern images were loaded onto a DELL 4310WX DLP data projector with a 1280×800 native resolution to project the patterns onto the target plane with a 60 Hz refresh rate. A Hamamatsu R7600U PMT was connected to a National Instrument data acquisition board to sample the PMT output (Figure 14b and c).

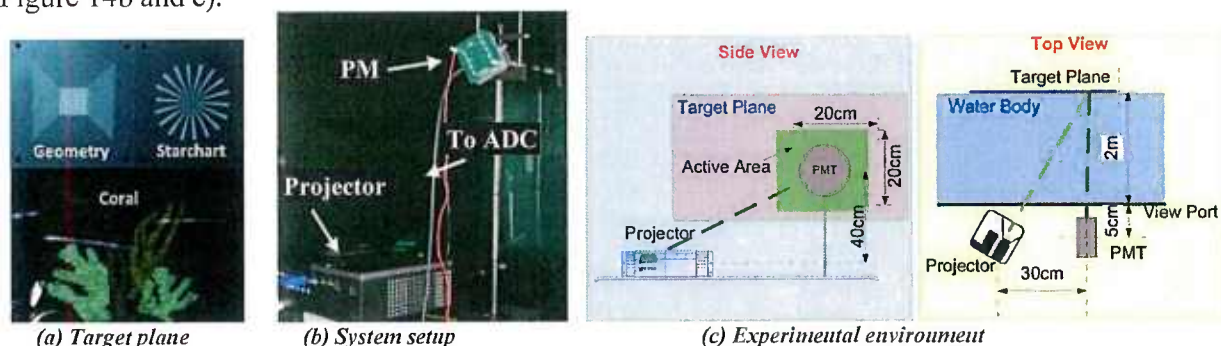
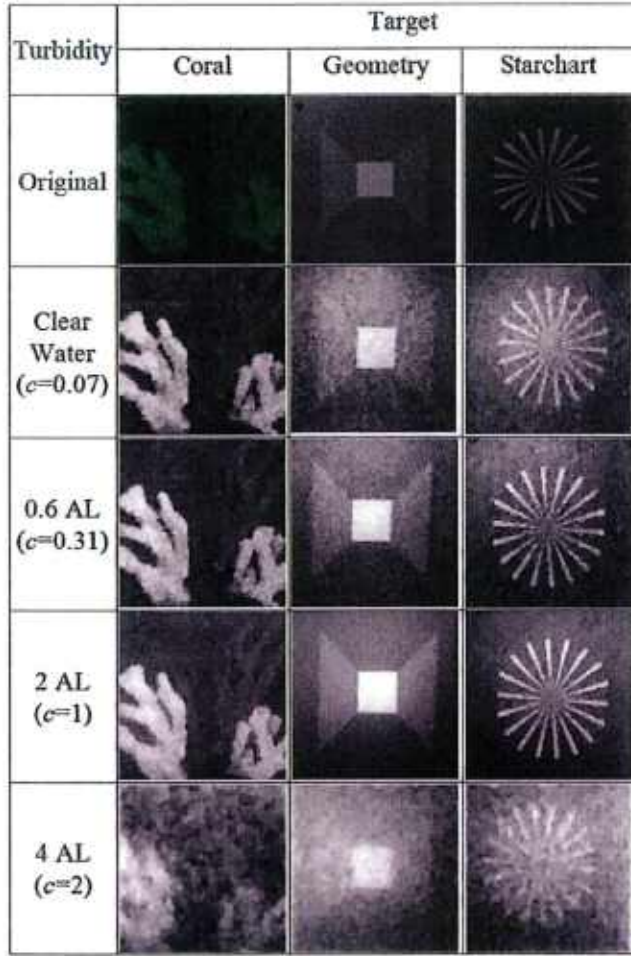


Figure 14. System setup geometry.

During the experiment, to achieve the necessary contrast for pattern projection, the projector was operated at a 20% brightness level with a light output of about 600 lumens. The dimensions of the measurement matrices were 100×100 pixels; the dimensions of the corresponding projected illumination patterns were 300×300 pixels, so that each element of the measurement matrix is covered with a 3×3 patch. With the distance between the screen and the projector set at 2 m, the on-screen active area is about 20×20 cm. Such an area is suitable for both technical targets (with a dimension of 14×14 cm) and most of the coral targets.

As shown in Figure 14c, there is a 30 cm separation between the projector and the PMT. Since the optical arrangement of the projector is such that the light is projected with an upward tilt (optimized for conference room use), the elevation of the PMT is 40 cm higher than the projector so that the center of the illuminated area is aligned with the FOV of the PMT. A bandpass filter with 5 nm full width at half maximum (FWHM) centered at 532 nm was placed in front of the PMT to retain only the green portion of the spectrum. The PMT had a wide FOV of 13 degrees. The experiment was conducted at four different turbidities: clear water,  $c = 0.31$ , 1, and 2.

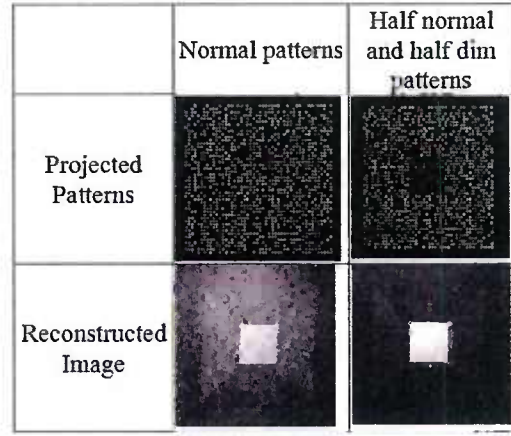




(a) Reconstructed image at different turbidities



(b) Reflection of the projected pattern from the corals.



(c) Dynamical pattern adjustment for contrast improvement.

Figure 15. (a) Reconstructed image at different turbidities (b) Reflection of the projected pattern from the corals and (c) Dynamical pattern adjustment for contrast improvement.

Figure 15a illustrates the reconstructed images at different turbidities. All images are at a resolution of  $100 \times 100$  pixels, and 2500 measurements were used in the reconstruction to give an effective compression ratio of 4:1. It can be observed that for the technical targets, the quality of the reconstructed images initially improves with increasing turbidity, though this trend breaks down at the highest turbidity of 4 AL (due to the power limitation of the illuminator). The main reason for the initial improvement was that the specular reflections from the surfaces of these two targets were reduced with increased turbidity. On the other hand, the coral results maintained fairly consistent quality at different turbidities, though this trend also broke down at 4 AL. While the center portion of the corals is clearly identifiable in the color image, the coral reflectivity at  $532 \text{ nm}$  (green light) is extremely low, as can be observed in Figure 15b, which results in a low-contrast image reconstruction of this region.

In general, the current implementation of the proposed approach seems to favor higher contrast regions of the image (as can be seen with the Geometry target in clear water as well). Additional work will be required to address this issue. One advantage of the CS approach is that the image reconstruction can begin when a minimum number of measurements are acquired, and image quality can then be progressively improved with additional measurements. Therefore, one potential approach



is to dynamically identify the high-contrast and low-contrast regions from initial reconstructions, and adjust the intensity of the projected patterns to accentuate the low-contrast regions. One such attempt for the Geometry target is shown in Figure 15c. To compensate for the high-contrast center block, half of the patterns were projected with the center square intentionally dimmed by 50%, which helped to improve the results in the low-contrast regions.

#### 4.2. Simulation and experimental results of the Compressive Line Sensing system

The simulation environment developed for the frame-based CS underwater imager (Figure 4) was modified for this simulation. The simulation parameters are listed in Table 1 below. During the simulations, *certain simplifications (i.e., adopting CW laser instead of pulsed laser, and ignoring the noise and motion jitters in the measurements for each line), and approximations (e.g., separable beam spread function kernels)* were assumed in the current, early stage of development and learning. As such, the laser power level and the DMD refresh rate are nominal values in the simulations. This allows us to concentrate on investigating the interference introduced by the vertical spreading discussed in Section 3.4. We have gained a certain level of understanding of the system noise performance from the study of the frame based system in section 4.1.

**Table 1. Simulation Parameters**

Target distance (m)	7m			
Turbidities	0.04 AL (clear water), 2.1 AL, 4.2 AL and 7 AL			
DMD based SLM	Contrast: 5000:1, Refresh Rate: 32KHz			
Target reflectance	Max: 0.15, Min: 0.05			
Target Dimension (m <sup>2</sup> )	0.75			
CW laser	Divergence: 1mrad, Power: 1W			
Image Dimension	512x512 (i.e. 1.5mm pixel resolution)			
Images tested:	USAF1951_b test chart; searock, fish and seabed natural images			
CS Sparsifying basis	Discrete Wavelet (CDF 9/7)			
CS Pattern ON-pixel spacing	8			
Raw Measurements	32	64	128	256
Compression Ratio	16:1	8:1	4:1	2:1
Corresponding platform speed (knots)	4	2	1	0.5
Receiver Aperture	CS	75mrad		
	LLS	15mrad		

It is interesting to evaluate the effectiveness of the *JSM-1* model in exploring the inter-line correlation. Figure 16 and 17 compares the reconstructed images and the reconstruction performances between the DCS based joint reconstruction (i.e.,  $gnum > 1$ ) and independent reconstruction ( $gnum = 1$ ). The different measurement rate/ $gnum$  pairs used in DCS based joint reconstruction simulations are: 32 meas/line &  $gnum = 15$ ; 64 meas/line &  $gnum = 7$ ; 128 meas/line &  $gnum = 4$ ; and 256 meas/line &  $gnum = 2$ . At the lowest measurement rate (32 measurements/line), the reconstructed images and the corresponding SSIMs generally confirmed the image quality improvement results from the joint reconstruction via DCS paradigm. Even though the SSIMs for the USAF1951\_b test chart were nearly the same, the jointly reconstructed images were perceptually better than the images reconstructed independently at this measurement rate. At higher measurement rates ( $> 64$  measurements/line), there was enough information to recover each line independently; however, joint recovery improved the overall image quality by reducing the line-to-line reconstruction quality variations. This can be observed by examining the SSIM curve of the fish test image in clear water (Figure 17e) for the case

where each line is recovered independently: the SSIM score with 256 measurements/line was even lower than that using 128 measurements/line.

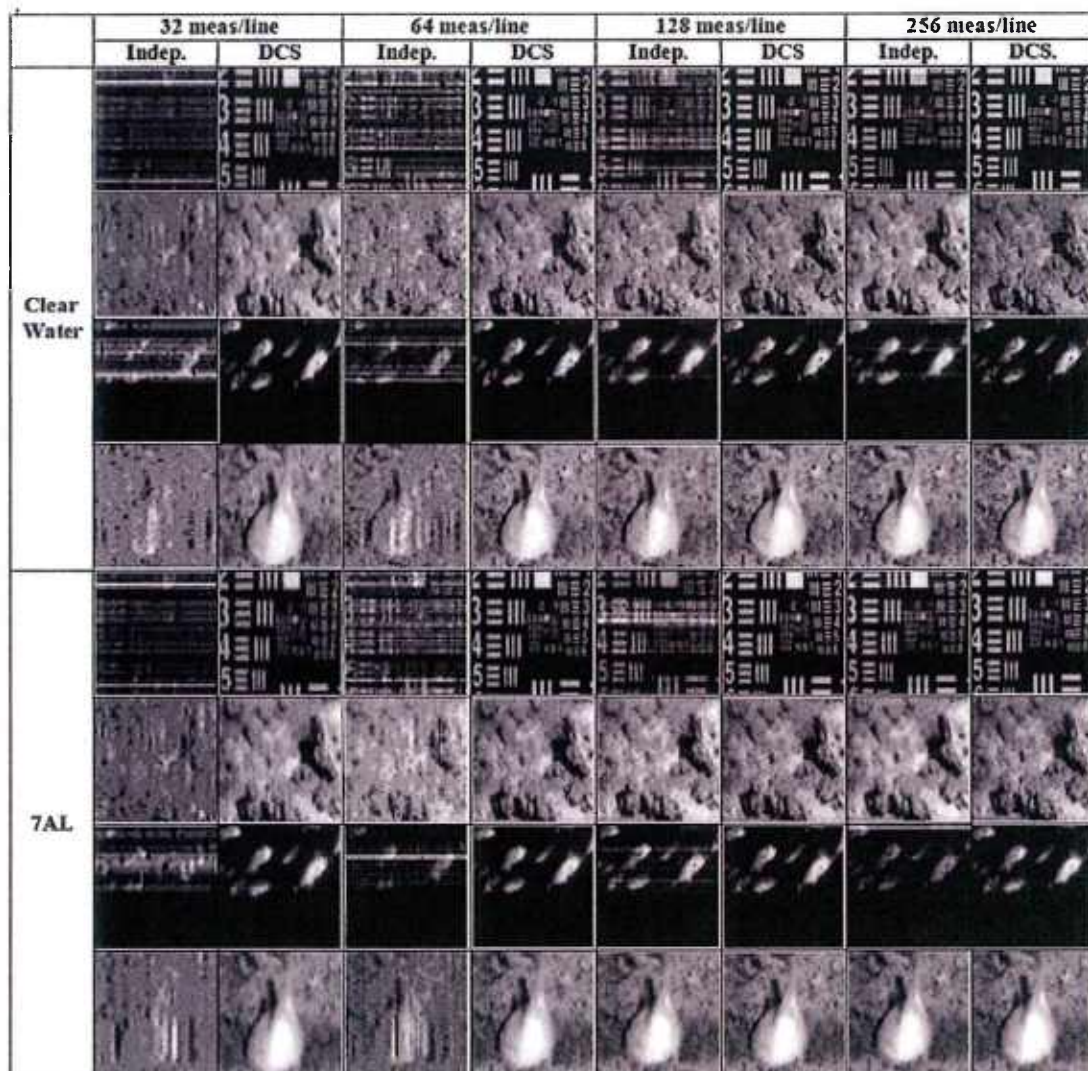
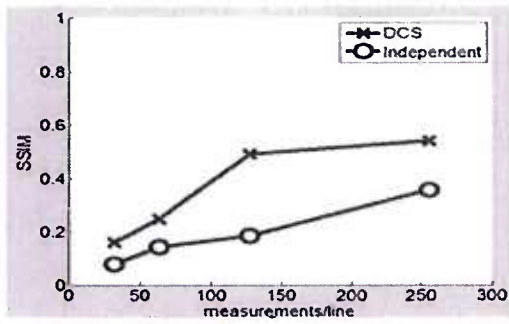
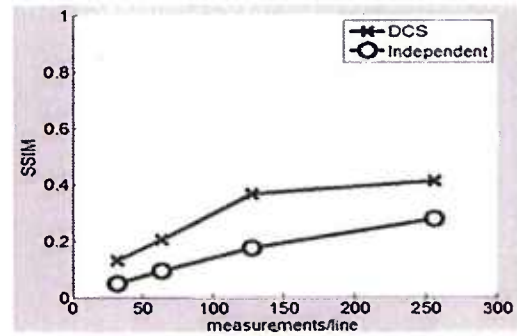


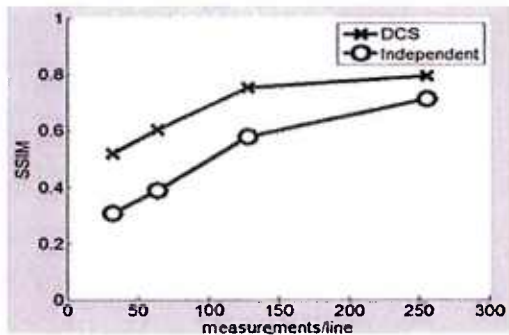
Figure 16. Comparison between LLS and CS Images with different measurements rates at different turbidities



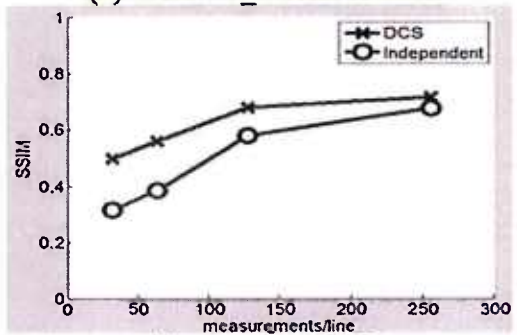
(a) usaf1951\_b chart in clear water



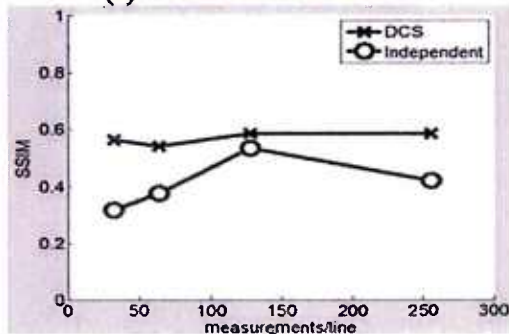
(b) usaf1951\_b chart at 7AL.



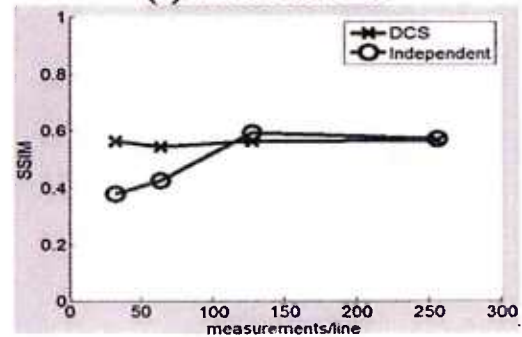
(c) searock in clear water.



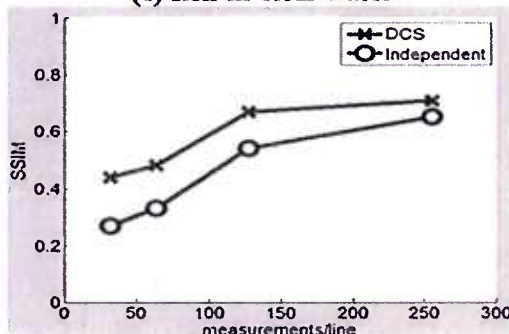
(d) searock at 7AL.



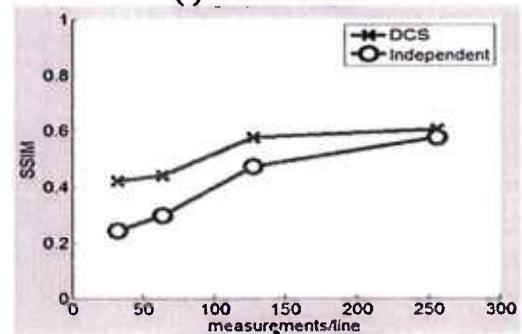
(e) fish in clear water



(f) fish at 7AL.



(g) seabed in clear water.



(h) seabed at 7AL.

Figure 17. Performance comparisons between joint reconstruction via DCS JSM-1 and reconstructing each line independently.



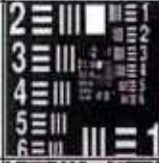



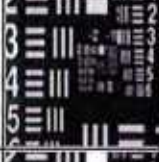



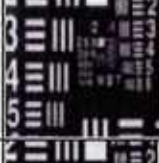



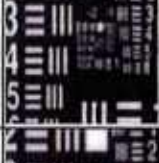



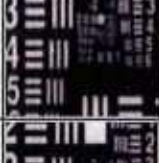
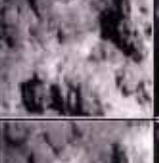






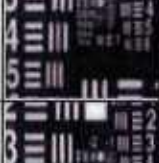





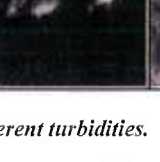

		Images			
		Usaf1951_b	searock	fish	seabed
Clear Water	LLS				
	CS				
2.1 AL	LLS				
	CS				
4.2 AL	LLS				
	CS				
7AL	LLS				
	CS				

Figure 18. Reconstruction images at different turbidities.

Figure 18 demonstrates the compressive line sensing imager performance against various test images at different turbidities. All images were reconstructed with 256 measurements/line (2:1 compression ratio) and  $g_{num}=2$ . The images from LLS simulations are also included. In Figure 19, the SSIM at various turbidities is presented.



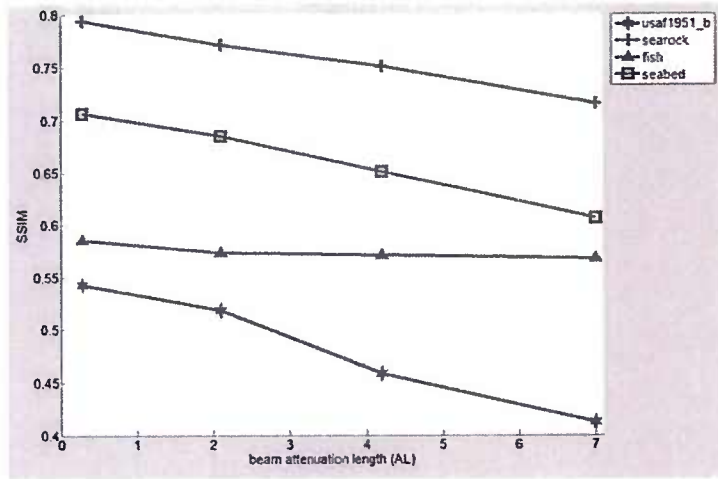
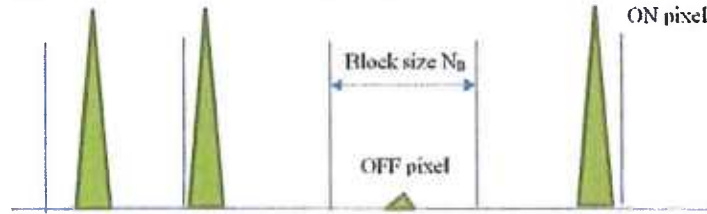


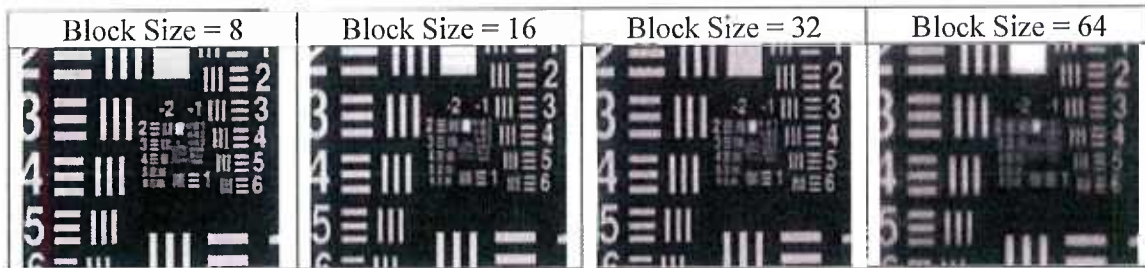
Figure 19. Reconstruction Performance at different turbidities (SSIM metrics).

It should be stressed, again, that all of the simulations were done without considering the noise induced image degradation. Under such assumption, the performance difference between pulsed LLS and CW LLS was also negligible. A more rigorous comparison between compressive line sensing imager and the LLS system will be conducted in future work.

Lastly, it is interesting to compare the image reconstruction with patterns with different top level block sizes. In the Compressive Line Sensing system, the block size is essentially the horizontal distances between two blocks (Figure 20a). Figure 20b shows the reconstructed image of usaf1951\_b in clear water using patterns with four different block sizes.



(a) Illustration of block sizes in Compressive Line Sensing Pattern



(b) Reconstructed Images using patterns with different block sizes

Figure 20. Reconstructed usaf\_1951b test chart in clear water using patterns with different block sizes

Since the horizontal dimension of the image is 512 pixels, the maximum number of ON pixels for a pattern with block size=8, 16, 32 and 64, the maximum number of ON Pixels will be 128, 64, 32 and 16 respectively. It is therefore very interesting that while there was some image degradation with increased block size, good fidelity was maintained even when the block size was increased to 64 – a very sparse pattern with maximum 16 ON pixels in each pattern. This feature can be very beneficial for

microwave and/or millimeter wave active serial imaging systems, where the Compressive Line Sensing is also applicable. In these systems, such sparse beam patterns can significantly reduce the complexity and cost of the antenna design.

#### Initial experimental results

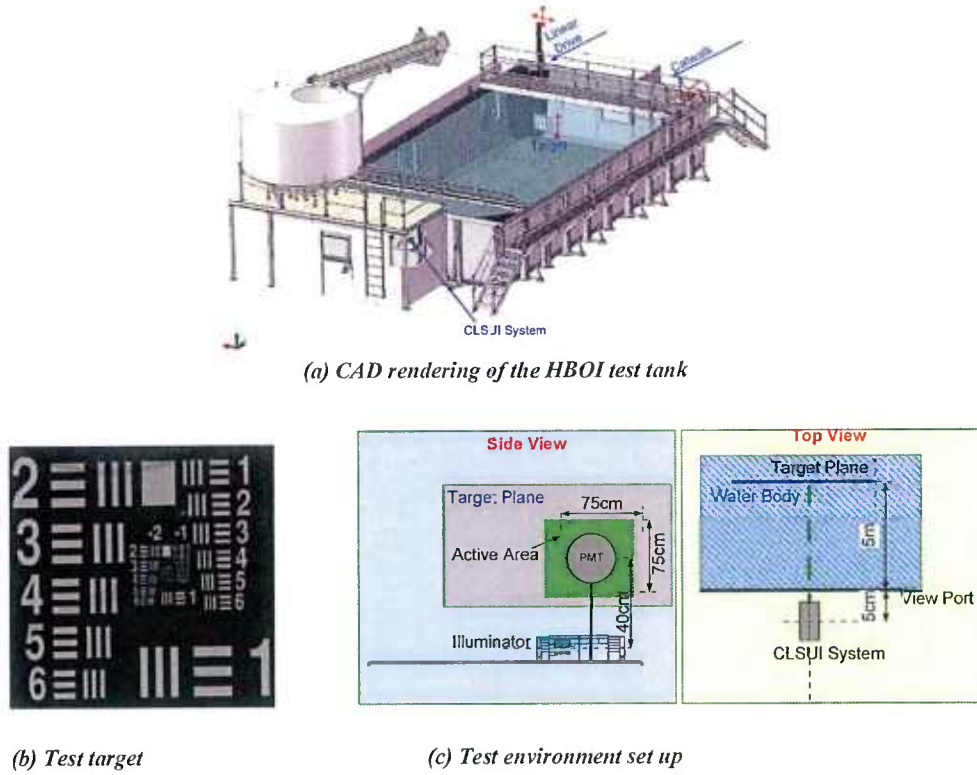


Figure 21. HBOI Optical Imaging Test Tank and test configuration

Initial validation tests of Compressive Line Sensing imager were conducted using the prototype system described in section 3.5 in the HBOI optical test tank under clear water ( $c=0.03 \text{ m}^{-1}$ ) conditions.

During the experiment, a  $75 \text{ cm}^2$  USAF1951-B target was placed 5 m away from the viewport. (Figure 21) The beam spot size was about 1.5 mm with a 512-pixel maximum pixel count. The DLP Lightcrafter was operated at a 250 Hz refresh rate (i.e., cycling through 250 patterns per second) during the tests due to the limitation of the current version of firmware. The same set of binary patterns  $\{A_m\}$  used to illuminate the target was fed into the EODES radiative transfer model with the system parameters (i.e., laser divergence, illuminator/receiver separation and target distance, etc.) and environmental conditions ( $c=0.03 \text{ m}^{-1}$ ) to predict the on-target measurement patterns  $\{\Phi_m\}$ . Equation (4) was then applied to  $\{\Phi_m\}$  and the corresponding PMT measurements  $\{y_m\}$  to generate the inputs needed to solve Equation (9) via the L1\_homotopy.

The prototype system is still a work-in-progress. However, some interesting experimental results using the current hardware are still worthy of some discussion. Figure 22a is the reconstructed image using 256 measurements per line (2:1 compression) with  $g_{\text{num}}=2$  lines, following the cost function in Equation (9). The right side of the image was quite dim indicating substantial light loss. The cause of this image quality degradation was traced to the imperfect illuminator design, mainly the non-uniform illumination of the DMD surface (Figure 22b). Direct compensation of the bias by dividing each line with the distribution curve in Figure 20b was not successful (Figure 22c).

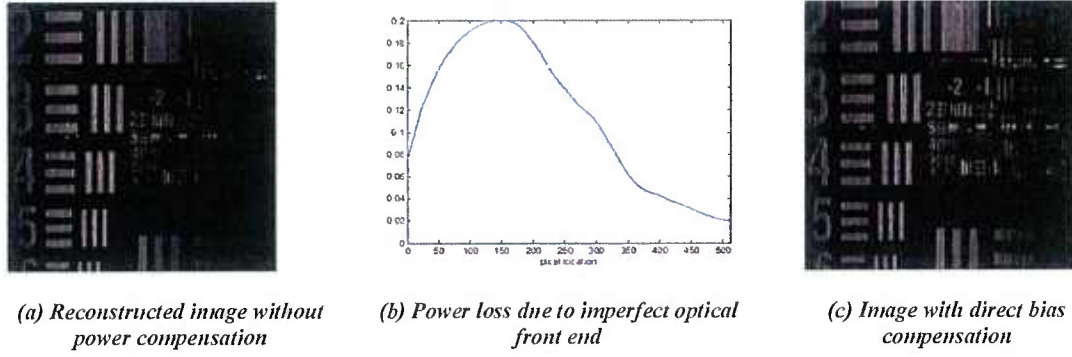


Figure 22. Initial image reconstruction and study of the uneven power distribution

Alternatively, to mitigate this issue the cost function Equation (7) was revised to account for the power distribution bias:

$$\begin{aligned} \alpha^* = \arg \min & \quad \|\alpha_c\|_1 + \|\alpha_1\|_1 + \dots + \|\alpha_L\|_1 \\ \text{subject to} & \quad \|\tilde{y}^B - (P_{bias} \tilde{\Phi}^B) \Psi \alpha\|_2 \leq \varepsilon \end{aligned} \quad (9)$$

where  $P_{bias}$  is the power distribution bias illustrated in Figure 22b. The reconstructed images based on Equation (9), with different measurement rates and line groups, are shown in Figure 23.

The image quality improvement using the bias compensated measurement matrix can be clearly observed by comparing Figure 22 and Figure 23. Albeit there was still an image quality difference between the left and right sides of the imagery. This could be regarded as a “self-repair” exercise in case of hardware deficiency/failure, a demonstration of the highly adaptive nature of the proposed compressive line sensing technique. Here again, the benefit of exploiting joint sparsity was evident as well (compare Figure 23c and Figure 23f).

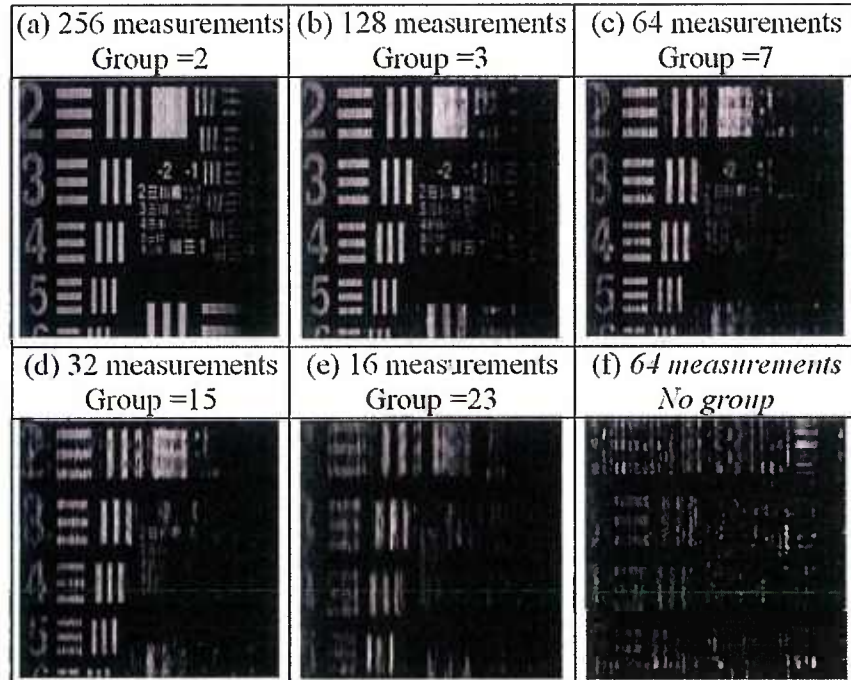


Figure 23. Image reconstruction using bias-compensated measurement matrices with different measurement rates and line grouping



## 5 CONCLUSIONS

Through the hard work of all the investigators participated in the research and with the guidance of the ONR program officers, the main objective of the project has been achieved. Extensive simulations and experimental studies were conducted through the course of this project. The research resulted in the publications of two peer-reviewed journal papers; multiple conference publications and one US patent filing. Through these activities, the basic framework of the Compressive Sensing based Electro-optical underwater active imaging system has been established. The most important outcome of this project is the Compressive Line Sensing concept. While the initial motivation is to target the underwater electro-optical system design, the paradigm of “sensing each line *independently* and reconstruct a group of lines *jointly*” is applicable in other mode of active imaging systems (i.e. microwave, millimeter wave imaging systems) or in different environments (i.e. airborne or space based sensing) as well. The multi-scaled measurement matrix design is especially attractive for microwave or millimeter wave imaging system. The sparse beams in the sensing patterns generated using this scheme can significantly reduce the cost and complexity of the antenna design in such imaging systems.

Another interesting discovery during the course of the study is the highly adaptive nature of the proposed active compressive sensing systems, both the frame based system and the Compressive Line Sensing system. Albeit in both cases, this feature was used to mitigate image quality, it is conceivable that more interesting applications can be derived as well, such as re-tasking the sensor to tracking different target priority on the fly. In this regard, the system shares some similarity with the feature specific imaging [7].

The gain from the lower sampling rate (i.e., lower speed/narrower bandwidth electronics, more compact and reliable system design, etc.) is common to many other CS applications. However, the proposed frame-based CS imager and the Compressive Line Sensing imaging system offer some additional features. While a CW laser is used in this initial effort to simplify the investigation, the compressive line sensing imaging system is compatible with a pulsed laser. In such a setting, *resource compression* translates into lower laser repetition rate, thereby reducing energy consumption and system cost and also improving the system reliability, critical for future long duration AUV/UAV deployments under stringent power constraints.

Going forward, significant work is required to optimize the Compressive Line Sensing system design. It is important to develop a more accurate joint sparsity model to better exploit the inter-line redundancy. It would also be of value to further increase the DMD refresh rates for such special patterns and to investigate other SLM devices such as the Grating Light Valve (GLV) [16], which is capable of faster refresh rates than the DMD. The impact of motion needs to be characterized. The noise characteristics and the impact from other environmental conditions, such as the ambient light, etc., need to be incorporated into the simulation. The current prototype system needs to be improved and enable a thorough experimental study of this concept through different turbidities.

## 6. REFERENCES

- [1] R.G. Baraniuk, “Compressive Sensing,” IEEE Signal Processing Magazine, vol. 24, pp. 118-121, 2007.
- [2] D. Baron, M. B. Wakin, M. F. Duarte, S. Sarvotham, and R. G. Baraniuk, “Distributed compressed sensing”, Rice University, Depart. Electrical and Computer Engineering Technical Report TREE-0612, Nov 2006.



- [3] E. Candes and J. Romberg, "Sparsity and Incoherence in Compressive Sampling," *Inverse Problems*, vol. 23, pp. 969-985, 2007.
- [4] E. J. Candes, M. B. Wakin, and S. P. Boyd, "Enhancing sparsity by reweighted L1 minimization," *Journal of Fourier Analysis and Apps*, vol. 14, no. 5-6, pp. 877-905, 2008.
- [5] D. Donoho, "Compressive Sensing," *IEEE Trans. Inform. Theory*, vol. 52, pp. 1289-1306, 2006.
- [6] M. A. Neifeld and P. Shankar, "Feature-specific imaging," *Applied Optics* 42(17), pp. 3379-3389, 2003.
- [7] D. Dudley, W. Duncan and J. Slaughter, "Emerging Digital Micromirror Device (DMD) Applications," *Proc. of SPIE*, 2003, 4985, 14-25.
- [8] T. E. Giddings and J. J. Shirron, "Numerical Simulation of the Incoherent Electro-optical Imaging Process in Plane-Stratified Media," *Opt. Eng.* vol. 48, no. 12, 126001 (2009).
- [9] T. E. Giddings, "Photomultiplier Receiver Model for Electro-Optical Systems", *Metron Tech. Rep.*, 2008.
- [10] T. J. Kulp, D. Garvis, R. Kennedy, T. Salmon, K. G. Cooper, "Development and testing of a synchronous-scanning underwater imaging system capable of rapid two-dimensional frame imaging," *Appl. Opt.* Jul 1;32(19):3520-30, 1993.
- [11] J. W. McLean, "High-resolution 3D underwater imaging," *Airborne and In-Water Imaging, Proc. SPIE*, vol. 3761, pp. 10-19, 1999.
- [12] B. Ouyang, F. R. Dagleish, F. M. Caimi, T. E. Giddings, J. J. Shirron, A. K. Vuorenkoski, W. Britton, B. Ramos and G. Nootz, "Compressive Sensing Underwater Laser Serial Imaging System", *Journal of Electronic Imaging*, special edition on Compressive Sensing, Vol. 22, Issue 2, 2013.
- [13] D. Rashkin, I. Cardei, M. Cardei F. R. Dagleish T. E. Giddings, "Detector Noise Model Verification for Undersea Free Space Optical Data Links", *Proc. MTS/IEEE Oceans'12*, 2012.
- [14] J. I. Trisnadi, C. B. Carlisle, and R. Monteverde, "Overview and applications of grating light valve based optical write engines for high-speed digital imaging", *Proc. SPIE-MOEMS Display Imag. Syst. II*, 2004, vol. 5348, pp. 52-64, 2004.
- [15] Z. Wang, A. C. Bovik, H. R. Sheikh and E. P. Simoncelli, "Image quality assessment: From error visibility to structural similarity," *IEEE Transactions on Image Processing*, vol. 13, no. 4, pp. 600-612, Apr. 2004.
- [16] A. D. Wyner and J. Ziv, "The rate-distortion function for source coding with side information at the decoder", *IEEE Transactions on Information Theory*, Jan, 1976.
- [17] D. Slepian and J. K. Wolf, "Noiseless coding of correlated information sources", *IEEE Trans. Inform. Theory*, vol. 19, pp. 471-480, July 1973.
- [18] M. Salman Asif and J. Romberg, "L1 Homotopy: A MATLAB Toolbox for Homotopy Algorithms in L1 Norm Minimization Problems", <http://users.ece.gatech.edu/~sasif/homotopy/>, retrieved on March 1, 2013.

## 7. RELATED PROJECTS

- A related project, "N00014-10-1-0914: HBOI Underwater Imaging and Communications Research – Phase II." was also being conducted with ONR grants during the study of the frame based Compressive Sensing concept.
- Another related project "Airborne Compressive Sensing Topographic Lidar" is being conducted under AFRL grant # FA9550-13-1-0107.
-

## **8. PUBLICATIONS ACKNOWLEDGING ONR GRANT N00014-12-1-0921**

### Journal Papers

- Ouyang B., Dalglish F. R. , Caimi F. M. , Giddings T. E. ,Vuorenkoski A. K. , Britton W. and Nootz G., “Compressive Line Sensing Underwater Imaging System”, Journal of Optical Engineering, special edition on Ocean Optics, April 2014.
- Ouyang B., Dalglish F. R., Caimi F. M., Giddings T. E., Shirron J. J., Vuorenkoski A. K., Nootz G., Britton W. and Ramos B., “Compressive Sensing Underwater Laser Serial Imaging System ”, Journal of Electronic Imaging, special edition on Compressive Sensing, Vol. 22, Issue 2, 2013.

### Conference Presentations

- Ouyang B., Caimi F. M., Dalglish F. R., Nootz G., Britton W., Vuorenkoski A. K., Compressive line sensing serial imaging system for the underwater environment”, SPIE DSS’14 (accepted).
- Ouyang B., Caimi F. M., Dalglish F. R., Vuorenkoski A. K., and Britton W., “(JEI Invited) Compressive sensing underwater active serial imaging systems”, IS&T/SPIE Electronic Imaging 2014.
- Ouyang B., Dalglish F. R., Vuorenkoski A. K., Caimi F. M., and Britton W., “Compressive line sensing underwater imaging system”, SPIE Proceedings Vol. 8717, 2013.

## **9. PATENT APPLICATION**

- Bing Ouyang, Fraser Dalglish, Anni Dalglish, US Application No.: 14/021,822, “MEMS Microdisplay optical imaging and sensor systems for underwater and other scattering environments”, September 9, 2013.